nature nanotechnology

SUPPLEMENTARY INFORMATION
https://doi.org/10.1038/s41565-018-0150-y

In the format provided by the authors and unedited.

Single entity resolution valving of nanoscopic species in liquids

Patric Eberle[1], Christian Höller[1], Philipp Müller[1], Maarit Suomalainen[2], Urs F. Greber[2], Hadi Eghlidi[1]* and Dimos Poulikakos[1]*

---

[1]Laboratory of Thermodynamics in Emerging Technologies, ETH Zurich, Zurich, Switzerland. [2]Institute of Molecular Life Sciences, University of Zurich, Zurich, Switzerland. [3]These authors contributed equally: Patric Eberle, Christian Höller *e-mail: eghlidim@ethz.ch; dpoulikakos@ethz.ch

Supplementary Information: Single entity resolution valving of nanoscopic species in liquids

Patric Eberle, Christian Höller, Philipp Müller, Maarit Suomalainen, Urs F. Greber, Hadi Eghlidi and Dimos Poulikakos

P.E. and C.H. contributed equally to this work.

*Correspondence to: Hadi Eghlidi (eghlidim@ethz.ch) or Dimos Poulikakos (dpoulikakos@ethz.ch)

<u>This Supplementary information contains:</u>

Supplementary Text

Supplementary Figures 1-13

Supplementary Video Captions

Supplementary References

Supplementary Text

Detailed force analysis for d.c. and a.c. mode

The stresses acting on the particles in the system investigated can be separated according to their hydrodynamic or electric origin and the resulting forces can be calculated by integration of the respective stress tensors over the surface area of the particle[1]. The force related to the presence of the electric field can be precisely evaluated using the Maxwell stress tensor and reads

$$\mathbf{F}_E = \varepsilon_0 \varepsilon_r \int_{\Omega} \left[\mathbf{E}\mathbf{E}^{\mathrm{T}} - \frac{1}{2}\left(\mathbf{E}^2\right)\mathbf{I} \right] \mathbf{n} dA , \qquad (10)$$

where ε_0, ε_r **E, I**, **n** and Ω are the absolute - and relative permittivity, the electric field, the identity matrix, the outer unit vector normal to the particle surface and the surface area of the particle, respectively.

Alternatively, for the system investigated here, the electric force $\mathbf{F}_E$ can be calculated using the Coulomb forces acting on the surface charges (electrophoretic) and the force related to the polarization (permittivity and conductivity) of the particle approximated with an induced dipole model (dielectrophoretic). F_{E} can be rewritten as

$$\mathbf{F}_E = \int_{\Omega} q_S \mathbf{E} dA - 2\pi\varepsilon_m R^3 \operatorname{Re}\left(\frac{\varepsilon_p^* - \varepsilon_m^*}{\varepsilon_p^* + \varepsilon_m^*} \right) \nabla |\mathbf{E}|^2 , \qquad (11)$$

where q_S and R are the surface charge density and the radius of the particle, respectively. The indices m and p denote medium and particle.

Using the hydrodynamic stress tensor one obtains the hydrodynamic force F_{H} exerted on the particle which arises due to spatial pressure variations in the fluid and due to the viscous drag when a fluidic flow is present past the surface of the particle.

$$\mathbf{F}_H = \int_{\Omega} \left[-p\mathbf{I} + \eta \left(\nabla(\mathbf{u}-\mathbf{u}_P) + \nabla(\mathbf{u}-\mathbf{u}_P)^{\mathrm{T}} \right) \right] \mathbf{n} dA \quad , \tag{12}$$

where p, η and $\mathbf{u}$ are the pressure, the dynamic viscosity and the velocity of the fluid, respectively. $\mathbf{u}_P$ is the velocity of the particle.

Fluid flow in our system can be induced by applying an external electric field on the nanoelectrodes. Such an electrokinetic driven flow can be analyzed by solving the coupled equations Poisson-Nernst-Planck (PNP) and Navier-Stokes (NS) with the relevant boundary conditions. For the hydrodynamic analysis using the NS equation, a body force

$$\mathbf{f} = \left(e\sum_{i=1}^{k} n_i z_i \right) \mathbf{E} - \left[\frac{1}{2} \mathbf{E}^2 \nabla \varepsilon_m \right] - \nabla \left[\left(\sum_{i=1}^{k} n_i + n_W \right) k_B T \right] \tag{13}$$

has to be considered, where n_i and z_i are the concentration and valence of the i-th ionic species, respectively. The three terms account for the Coulomb interactions between the ions and the electric field (first term), the dielectric force (second term) and the osmotic pressure (third term)[2,3]. Since $\left(\sum_{i=1}^{k} n_i + n_W \right) \approx const$ in the electrolyte, the osmotic pressure term (third term) in the body force equation can be neglected at uniform temperatures ($\nabla T = 0$).

Local heating of the fluid can give rise to permittivity and conductivity gradients and can induce an electrothermal related flow in the system[2]. Permittivity and conductivity gradients affect the Coulomb and the dielectric terms in the body force equation. Reference[2] presents an equation, which expresses the first two terms of the body force equation as a function of the temperature gradient for small changes in the charge density and electric field.

d.c. Mode

For the d.c. mode, the dielectrophoretic force (second term in the equation of the electric force $\mathbf{F}_E$) is several orders of magnitude smaller than the surface charge driven Coulomb forces (first term) for the particles investigated here and, hence, can be neglected.

The applied potential at the nanoelectrodes affects the local ionic concentrations and the electric field in the system. The electric field gives rise to a Coulomb body force (first term in body force equation) and may lead to d.c. electroosmosis. To precisely investigate the electric field and the fluid flow when a potential is applied at the nanoelectrodes, we solved the coupled PNP and NS equations for the trap-in-channel system in a 50 µm long nanochannel. The results are presented in Supplementary Fig. 10. Based on this simulation, we estimated the Coulomb, pressure related and viscous drag forces acting on a gold nanoparticle with 100 nm in diameter and a representative surface charge of 150*e.* The results show that the viscous drag and pressure related forces are about an order of magnitude smaller than the Coulomb force stemming from the surface charge. For the other particles discussed in the manuscript this ratio is within the same order of magnitude and, therefore, the osmotic flow can be neglected with good approximation for the verification of the experimental results.

Concerning the viscous drag, it should be pointed out that the viscous friction is enhanced when the particle travels along the walls with a separation of the order of the particle size[4]. The viscous friction in confined geometries is further increased when the double layers of particle and channel walls overlap. For example, Eichmann *et al*[5] shows a reduction of up to ~50% of the diffusivity of the particle, which is attributed to an enhanced electroviscous effect (EVE) due to the disruption of the local fluid velocity by counter ions in the diffusive part of the double layer.

An increase in viscous friction decreases the diffusivity and mobility of the particle and manifests itself by slowing down the passage of the particle through the valve. However, in our work, we do not study specifically the passage times of the particles and therefore, we do not need to consider the above-mentioned effects. Note that the viscous friction does not enter as a factor in the Boltzmann distribution formula, and therefore, theoretically, it does not affect the predicted probability distribution of the position of a particle in the equilibrium situation.

In the manuscript, we calculated the potential energy profile of the particle with an alternative energy-based approach. The nanovalve without applied potential can be modeled as a closed system, for which the following thermodynamic energy balance $U_{el} - T\Delta S = -W$ holds, where W is the mechanical work on the particle. Energy can be converted from the electrostatic energy in the electrolyte (U_{el}) and from the thermal energy of the surrounding ($T\Delta S$) to mechanical work and in opposite direction, whereby the amount of converted energy equals to the change in free energy F. It is obvious that W is equal to the potential energy of the particle and, hence, $U_P = F$. The effect of the applied potential is then considered as an additional (second) term in the equation of the potential energy of the particle ($U_P(\mathbf{r}_P) = F(\mathbf{r}_P) + z_p e\varphi(\mathbf{r}_P)$). The force exerted on the particle can be obtained by $-\partial U_P / \partial \mathbf{r}_P$, where $\mathbf{r}_\mathrm{p}$ is the coordinate of the particle. In this method, we do not account for the variations in ionic concentrations due the externally applied potential at the nanoelectrodes. However, it is shown in the manuscript that this is sufficient to explain the experimental results. Supplementary Fig. 10 also shows that the free energy based method is in acceptable agreement with the potential energy function of the particle obtained from solving PNP and NS equations for the case of applied potential.

The electrothermal flow can be neglected for the d.c. mode. This can be explained by the negligible temperature rise from Joule heating due to the very small current densities. A detailed analysis is not needed since even for the a.c. mode with much higher current densities the effect of the electrothermal flow can be neglected (see a.c. mode below).

a.c. Mode

In the a.c. mode, the estimated particle displacement at the employed frequency f = 10 MHz due to surface charge related Coulomb force is of the order of Angstroms which is much smaller than the relevant particle sizes. The first term in the electric force equation is therefore neglected for the a.c. mode and the dominant term is the dielectrophoretic force. For the a.c. mode, it is useful to define the time-averaged force

$$\langle \mathbf{F}_{a.c.} \rangle = -2\pi\varepsilon_m R^3 \,\mathrm{Re}\left(\frac{\varepsilon_p^* - \varepsilon_m^*}{\varepsilon_p^* + \varepsilon_m^*} \right) \nabla \left| \mathbf{E}_{a.c.} \right|^2 \tag{14}$$

using the root-mean-squared (rms) electric field $\mathbf{E}_{\text{a.c.}}$. Concerning the fluid flow, the first term in the body force equation (Coulomb force) can give rise to a.c. electroosmosis, which could induce a disturbing fluid flow in our system. a.c. electroosmosis is induced by the double layer at the electrodes and an electric field tangential to it[2]. However, with the separation of the electrodes in our system (d = 3 µm) and the employed frequency f = 10 MHz the formation of the double layer at the electrodes is practically inhibited. The characteristic double layer relaxation time $\tau_c = \frac{\kappa^{-1} d}{D}$ is of the order of µs, which is much larger than $1/f$ = 100 ns . Hence, we can neglect a.c. electroosmosis in our theoretical analysis.

The Joule heating in the electrolyte is for the a.c. mode clearly larger than for the d.c. mode and a careful analysis of the electrothermally induced fluid flow was performed. For an order of magnitude estimate, we solved the set of equations (5)–(7) and the heat transfer equations to obtain the temperature distribution in the trap-in-channel system for the extreme case at $V = 3$ $\mathrm{V}_{\mathrm{a.c.}}$ applied at the center electrode in combination with maximum ionic strength $I \approx 160$ mM (physiological conditions 1X PBS). Temperature variations in the fluid can induce gradients in its permittivity and conductivity giving rise to an electrothermal related body force[2]. Using the obtained temperature distribution and the body force equation for temperature gradients presented in reference[2] we solved the NS equation for the low Reynolds regime (laminar flow). In the body force equation we used the parameters $\alpha = -0.4$ %/K and $\beta = 2$ %/K according to reference[2]. The calculated fluid velocities were of the order of 10^{-9} m/s (Supplementary Fig. 12) which corresponds to a drag force of the order of 10^{-18} N for a particle with 100 nm in diameter using Stokes drag. This is about five orders of magnitude smaller than the repelling force induced by a closed valve ($\approx 10^{-12}$ N) and, hence, we can neglect the electrothermal related body force for the a.c. mode.

Summarized, for the verification of the experimental results in this study the effect of the fluid flow can be neglected with good approximation for both a.c. and d.c. mode and for the prediction of the particle position the following potentials energies can be used:

	Potential Energy of Particle
d.c. Mode	$U_P(\mathbf{r}_P) = F(\mathbf{r}_P) + z_p e\varphi(\mathbf{r}_P)$
a.c. Mode	$\langle U_P \rangle = -2\pi\varepsilon_m R^3 \operatorname{Re}(CM)\lvert\mathbf{E}_{a.c.}\rvert^2$

Reusability and large scale integration of the devices

The (reusable) chips were normally used for several days of experiments, and with one batch, several devices were generated (54 devices were fabricated per 4” silicon chip, each device with up to 18 parallel nanochannels with embedded nanovalves) with more than 70% yield of successful devices. The individual addressability and silicon-based fabrication of the nanovalves, enables their use as the basic blocks of nanofluidic systems, similar role to that of transistors in electronics or microvalves in microfluidics. They act as switches to allow or stop the passage of nanoparticles, can be controlled individually and independently, and, as shown with the two examples in the manuscript (trap-in-channel and trap-in-junction), can be combined on a chip to achieve modular design and various functionalities. More complex functionalities, such as memory or multi/de-multiplexing, can be achieved similarly to their microfluidics counterparts[6,7] leading to large-scale integration of chip-based nanofluidic devices. Such systems can be used for sorting, combining, isolating, and in-situ investigating various nanoscopic objects including macromolecules.

Design and electrochemical characterization of nanoelectrodes

We passivated the top surface of the nanoelectrodes, which consist of a Cr film, with a 2 nm thin layer of SiO_2, to suppress hysteresis in the I-V curve and retard water decomposition[8–10]. Such a thin insulation layer is known to increase the electrode-electrolyte electric contact resistance[11]. Supplementary Fig. 9 shows the cyclic voltammogram (I-V measurements) of a SiO_2 passivated Cr film electrode (material layer stack: Cr/Au/Cr, 25/25/20 nm) in different electrolytes. Cyclic voltammetry was performed at a voltage sweep rate of 50 mV/s using a three electrode cell incorporating a platinum counter, an Hg/Hg_2SO_4 reference electrode, and a SP300 potentiostat (BioLogic Science Instruments, Grenoble).

The SiO_2 passivated electrodes have negligible hysteresis as (Supplementary Fig. 9) and electrochemical water dissociation was retarded up to a potential difference (electrochemical window) of ~2.2 V. The onset of electrolysis imposes essentially an upper limit for the applied potentials in the a.c. mode. In the a.c. mode (10 MHz) our experiments did not show any nascent bubble formation due to water dissociation for voltages up to ~5 V at 1X PBS concentration. In the d.c. mode, when the valve is open, a potential pulse exceeding the electrochemical potential window (the potential range where no electrochemical reaction takes place) is needed in order to induce Faradaic current in the valve. This pulse is only applied during a very short time window of ≈ 20 ms in order to move the particle through the channel constriction. In the closed state of the valve, the ground potential is applied to all the electrodes and no Faradaic current is present. Similar to the a.c. mode, no nascent bubble formation was observed in the d.c. mode, in the range 3 – 5 V of applied potentials. This can be attributed to the fact that in small geometries gases dissolve in the liquid.

Correction for finite exposure time

The experimentally determined apparent mean square displacement of a particle $\left\langle \Delta\overline{\mathbf{x}}_p^2\left(t_{\mathrm{exp}}\right)\right\rangle$ in a potential well can deviate from the true mean square displacement $\left\langle \Delta\mathbf{x}_p^2\right\rangle$ due to the finite exposure time[12]. The ratio $\left\langle \Delta\overline{\mathbf{x}}_p^2\left(t_{\mathrm{exp}}\right)\right\rangle / \left\langle \Delta\mathbf{x}_p^2\right\rangle$ can be calculated with equation 14 in reference[12] as a function of the ratio of $t_{\mathrm{exp}} / \tau_R$. τ_R is the characteristic position relaxation time of the particle in the well and is given by $\tau_R = \frac{6\pi\eta r}{k}$, where η and r are respectively the dynamic viscosity and the radius of the particle, and k is the spring constant of a harmonic oscillator model of the well[13]. The relaxation time can be rewritten as $\tau_R = \frac{6\pi\eta r}{k_B T} s^2 = \frac{1}{D} s^2$, where D is the diffusivity and s is the standard deviation of the true particle displacement distribution in the potential well ($s = \left\langle \Delta \mathbf{x}_p^2 \right\rangle^{0.5}$).

For the measurement of the lateral displacement of a polystyrene bead (100 nm in diameter) in the trap-in-channel structure in a.c. mode at t_{exp} = 5 ms (Fig. 3a), we obtain:

Supplementary Table 1. Correction Factors.

	$\left(\left\langle \Delta \overline{\mathbf{x}}_p^2 \right\rangle / \left\langle \Delta \mathbf{x}_p^2 \right\rangle \right)^{0.5}$	τ_R	s
0.1X PBS	0.60	1 ms	51 nm
1X PBS	0.76	1.8 ms	68 nm

In the a.c. mode, the particle is forced in direction of the upper wall as the potential energy of the particle increases by ~$0.5 k_B T$ per 20 nm in negative z-axis direction. Therefore, the particle diffuses laterally in the trap in close proximity to the upper wall and its diffusion can become hindered due to the increased Stokes drag along and close to the walls. For a separation distance of almost 20 nm between particle and the upper wall, the near-wall hindered diffusion coefficient of the particle was determined to be $D_H \approx 0.59D$ (accounted in the calculation of Supplementary Table 1).

Joule heating in the nanovalve

The effect of joule heating was investigated by a simulation (COMSOL) of the temperature distribution in the cross section of the nanovalve using a heat source $Q_h = 5*10^{12}$ W/m^3 in the electrolyte[14]. The value for the heat source ($Q_{\mathrm{h}} = 0.5*\sigma\mathbf{E}^2$) is selected conservatively assuming 1X PBS concentration ($\sigma_m = 1.7$ S/m) and $|\mathbf{E}_{a.c.}| = 1$ V/μm , which represents the worst-case scenario. Supplementary Fig. 13 shows the obtained distribution of the temperature increase. The resulting maximum temperature increase in the channel is < 0.2 K. This negligible rise in temperature ensures that biological species investigated in the proposed system will not be harmed.

The effect of electrothermally induced fluid flow on the particle was also investigated by simulations[2]. The detailed analysis presented in the Supplementary Text and Supplementary Fig. 12 shows that the drag force from the electrothermally induced fluid flow is about five orders of magnitude smaller than the repelling force induced by a closed nanovalve.

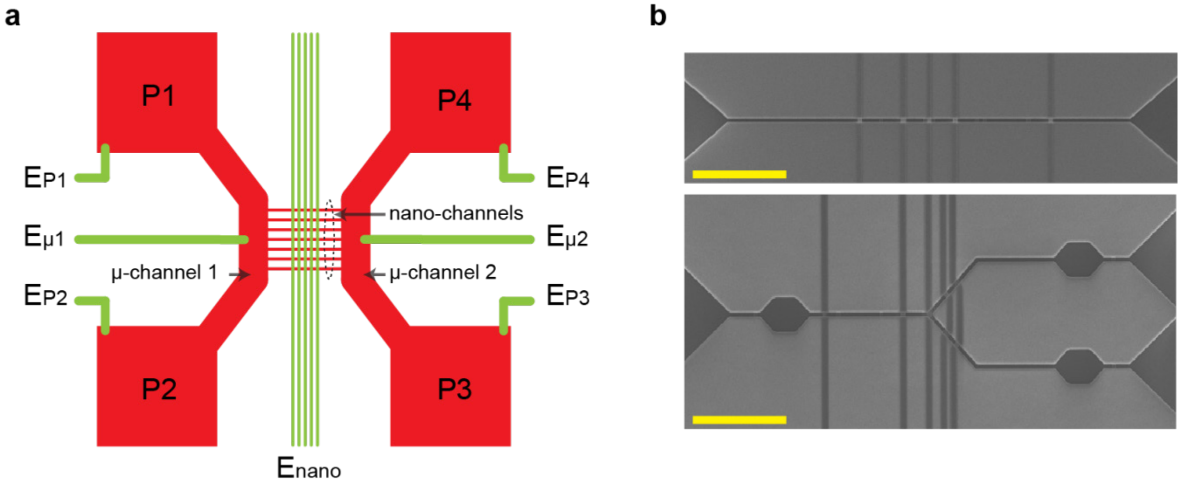

Supplementary Fig. 1. Schematics of the chip and electron micrographs of the nanochannel designs. a, Design of the fluidic chip comprising four fluidic ports (P1-P4), two microchannels (μ-channels) each connecting two fluidic ports, an array of nanochannels connecting the two μ-channel branches, and electrical connections to the electrodes in the ports (E_{P1}-E_{P4}), the μ-channels ($E_{\mu 1}$ and $E_{\mu 2}$) and the nanochannels (E_{nano}). **b,** Scanning electron micrographs show the nanochannel designs of the trap-in-channel and trap-in-junction structure. Here, the horizontal lines are the nanochannels and the five vertical lines crossing the nanochannels are the nanoelectrodes. Scale bars show 10 μm.

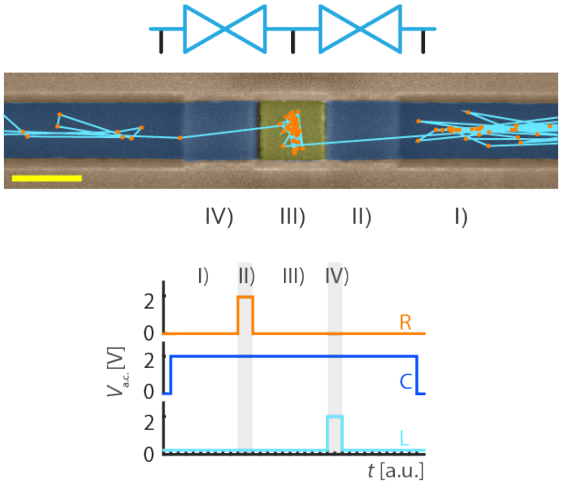

Supplementary Fig. 2. Guiding, confining and releasing lipid vesicles. Lipid vesicle (100 nm in diameter) guided in a.c. mode in buffer solution 0.1X PBS ($I \approx 16.2$ mM) within a trap-in-channel structure ($V_{a.c.} = 2$ V, $\mathbf{E}_{\mathrm{a.c.}} \approx 900$ mV/µm within the constriction of a closed valve). Lipid vesicle (I) comes from right and is stopped before the potential energy barrier of the right nanovalve, (II) moves through the right nanovalve (potential energy barrier of right valve removed), (III) is confined within the interspace between the two constrictions (right potential energy barrier restored), and (IV) moves through the left nanovalve (left potential energy barrier removed). Trajectories overlaid on top of SEM images and time-trace diagrams show electrode voltages for each step. Scale bar shows 500 nm.

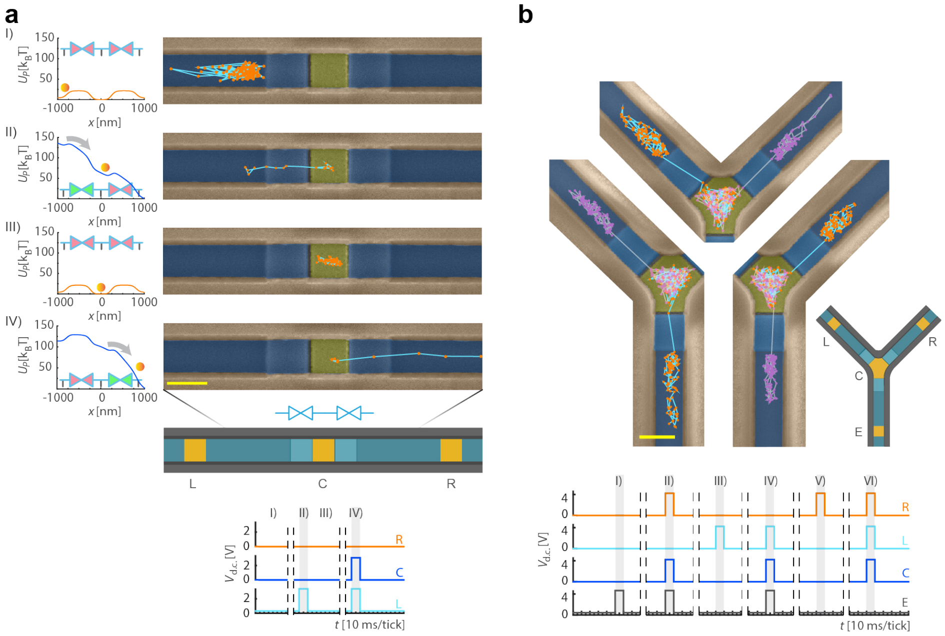

Supplementary Fig. 3. Guiding, confining and releasing gold nanoparticles in d.c. mode. a, A spherical 100-nm (diameter) gold particle (surface charge: ∼−150*e*) guided in d.c. mode in a trap-in-channel configuration at $I = 0.05$ mM ($V_{d.c.} = -3.5$ V, $\mathbf{E}_{d.c.} \approx -12$ mV/µm within the constriction of the actuated valve). Particle is (I) stopped before the potential energy barrier induced by the left nanovalve, (II) moved through the constriction of the left valve by modulating the potential energy, (III) confined in the interspace, and (IV) released through the right nanovalve. When the potential energy is bent to move the particle through the left valve (II), the potential energy barrier of the right valve remains sufficiently high $\Delta U_P \approx 5k_BT$ to stop the particle. **b,** A 60-nm (diameter) gold particle (surface charge: ∼−75*e*) is moved in a trap-in-junction device in d.c. mode in a sequence (I-VI) at $I = 0.05$ mM. Sequence of motion: bottom-center-left-center-right-center-bottom ($V_{d.c.} = -4.5$ V, $\mathbf{E}_{\mathbf{d.c.}} \approx -50$ mV/µm within the constriction of the actuated valve). (a and b), $V_{d.c.}$ was applied for a time period of 20 ms. This time period was selected to be sufficiently long, so that the particle can overcome the reduced potential energy barrier $\Delta U_P \approx k_BT$ of the open valve and move through the valve. Scale bar shows 500 nm.

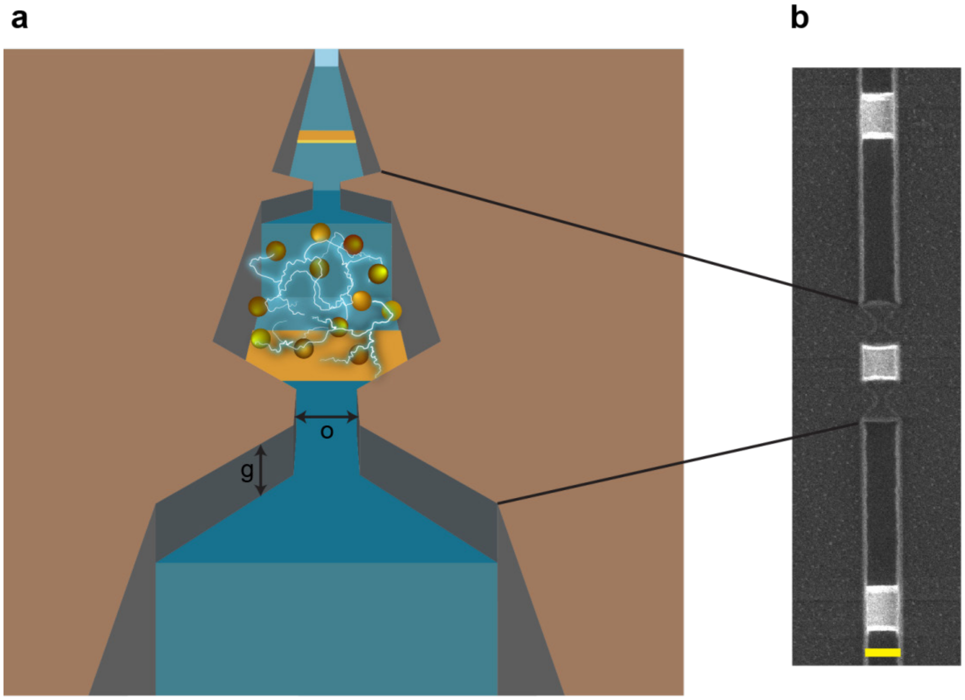

Supplementary Fig. 4. Trap-in-channel structure with bow-ties on top of larges steps. a, Schematic illustration showing the trap-in-channel structure for the QD experiments, with the further shrunk cross section of the channel constriction to o = 70 nm (width) and g = 40 nm (height). A trapped quantum dot is schematically shown between the two constrictions. **b,** SEM image of the same fabricated structure. Scale bar shows 500 nm.

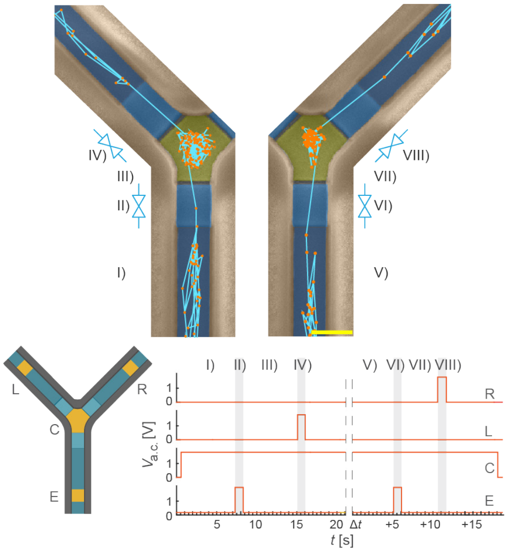

Supplementary Fig. 5. Guiding, confining and releasing adenoviruses. On-demand loading and releasing of single adenoviruses to the left (sequences I-IV) or right (sequences V-VIII) channels in trap-in-junction by switching potential energy barriers ($V_{a.c.}$ = 1.75 V, $\mathbf{E}_{\mathbf{a.c.}}$ ≈ 800 mV/µm) on and off in a.c. mode in 0.2X PBS ($I \approx 32$ mM). Trajectories are overlaid on top of SEM images, and time-trace diagrams show electrode voltages for each step. Scale bars show 500 nm.

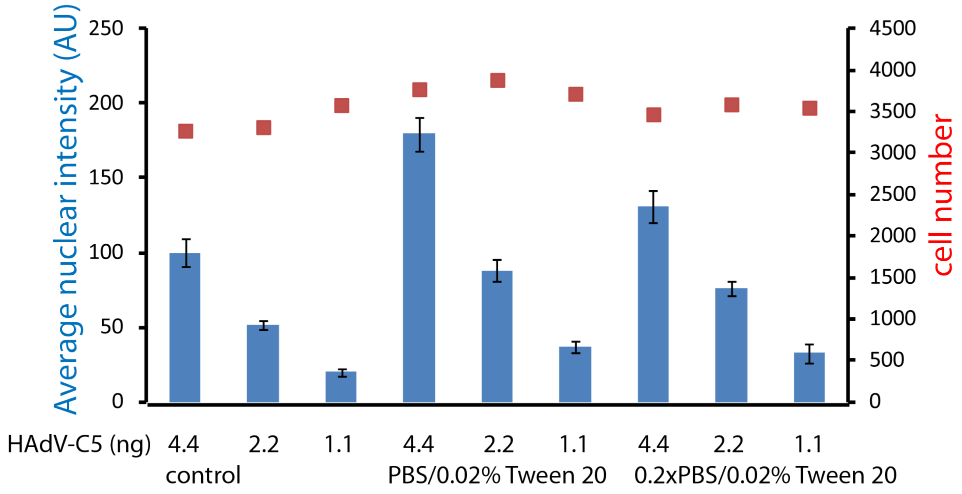

Supplementary Fig. 6. HadV-C5 retains infectivity in the assay buffer. HAdV-C5_EGFP virus was incubated in PBS/0.02% Tween 20 or 0.2xPBS/0.02 % Tween 20 buffer for 5 hours at room temperature, and then diluted into A549 growth medium for infection with the indicated amounts of input virus. Control infection was without virus pretreatment. The infected A549 cells were fixed 24 hours post infection, DAPI stained, and imaged by automated fluorescence microscopy. The average intensity of EGFP over a DAPI mask was quantitated and normalized to that of control infection with 4.4-ng input virus. The values represent mean values from three technical replicates (error bars show standard deviation). Cell numbers indicate mean cell numbers analyzed per technical replicate.

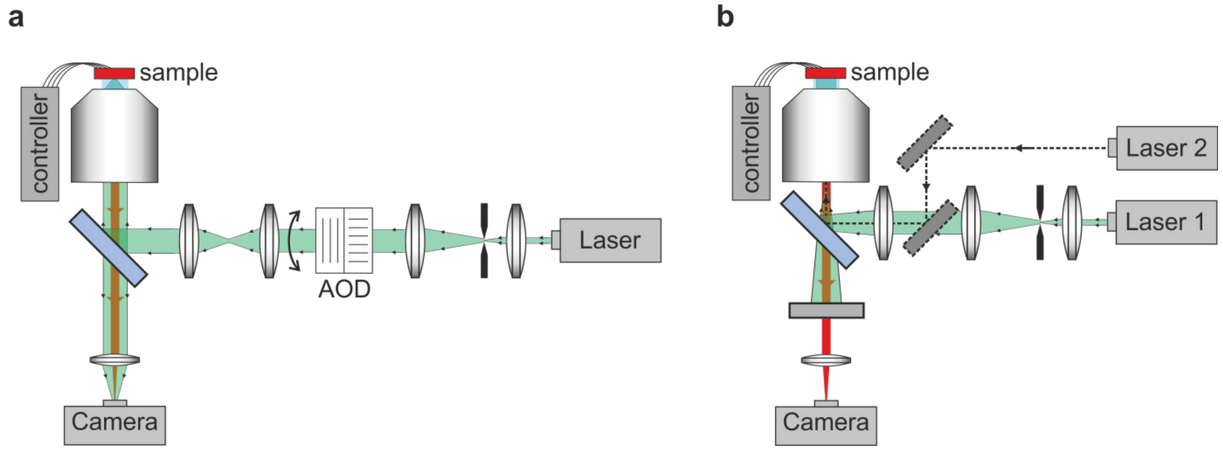

Supplementary Fig. 7. Schematics of the inverted microscope measurement setups. a, Interferometric scattering (ISCAT) setup for imaging metallic particles. The beam of a diode pumped laser (wavelength 532 nm) was deflected by an acousto-optical deflector (AOD) to scan the field of view through a 100X, 1.3 numerical aperture (NA) oil immersion objective focusing the light at the particle/sample plane. A CMOS camera (MV-1024-160-CL, PhotonFocus) measured the collected interferometric light from the particle and the SiO_2/Si interface (reflected light). **b,** Fluorescence setup for imaging fluorescent beads, lipid vesicles, viruses and quantum dots in standard wide field configuration. The fluorescent light was collected by a 100X, 1.4NA oil immersion objective and measured by a scientific CMOS camera (Andor Zyla 4.2 sCMOS) or a highly sensitive EMCCD (iXon Ultra 888). For excitation removal long-pass filters were inserted in the detection path.

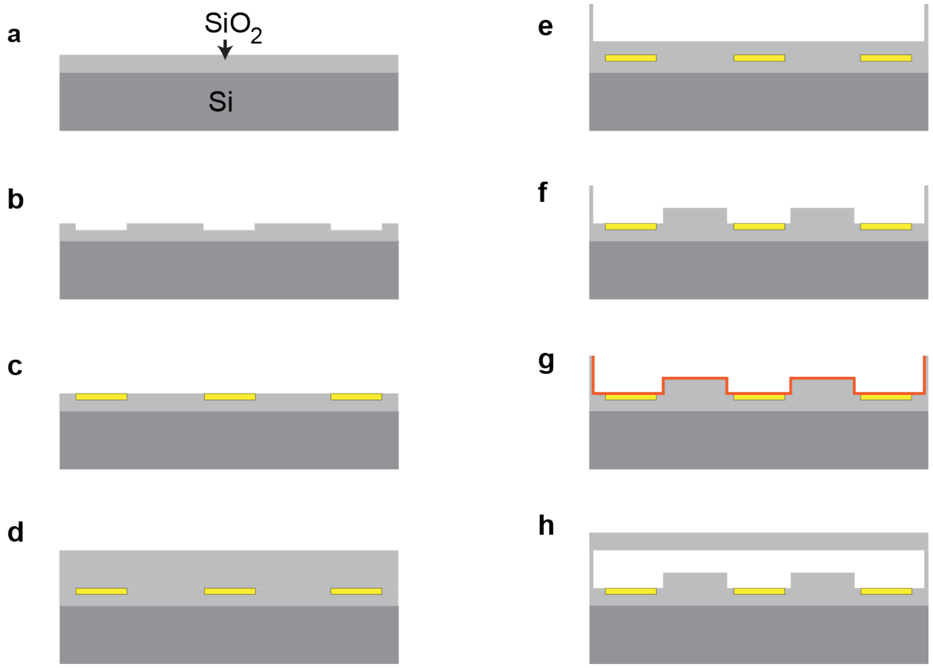

Supplementary Fig. 8. Fabrication sequence of the device. a, An initial SiO$_2$ layer was deposited on a clean Si wafer. **b,** Trenches were etched to accommodate the metal nanoelectrodes deposited by evaporation (**c**)**. d,** A second layer of SiO$_2$ was grown on the top facet in which the channels were etched with an initial depth (**e**). **f,** A subsequent dry etch process deepened the channels down to the nanoelectrodes and regions in the channel excluded from the etching, i.e. masked by the resist, formed the geometrical steps. **g,** Deposition of a 2 nm thin SiO$_2$ layer for electrochemical passivation of the nanoelectrodes. In the last step **h** the channels were closed and sealed by anodic bonding of a glass slide to the top facet of the structure.

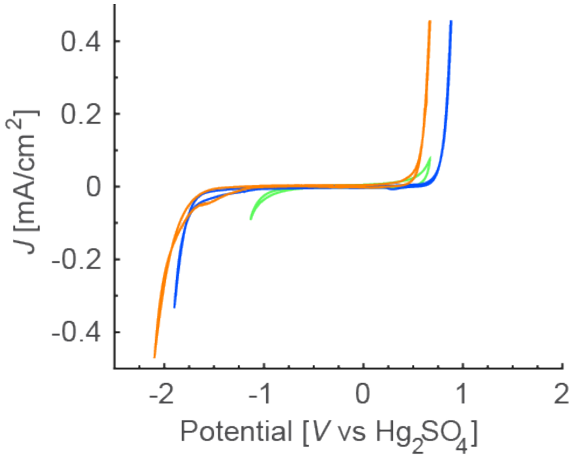

Supplementary Fig. 9. Cyclic voltammogram of nanoelectrode materials. I-V measurements of the Cr-film electrodes (material layer stack Cr/Au/Cr, 25/25/20 nm) passivated by a 2 nm thick SiO_2 layer measured in 0.05 mM KCl aqueous solution (blue solid line) and in 1X PBS solution (orange line). For reference, the I-V measurement of the Cr electrode (green line) measured in DI water is also given. The I-V relation $J(V) = ae^{bV} - ce^{-dV}$ [15] fitted to the DI water measurements was used for the d.c. mode simulations.

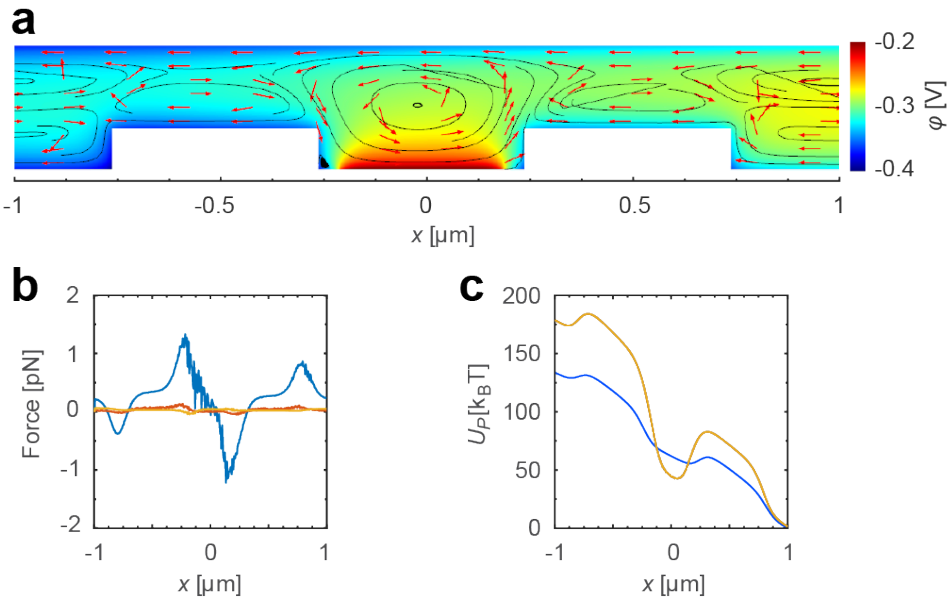

Supplementary Fig. 10. Electrokinetic analysis of the trap-in-channel system in d.c. mode. A 2D model of the coupled Poisson-Nernst-Planck (PNP) and Navier-Stokes (NS) equations for the trap-in-channel system the electric potential φ and fluid flow was solved numerically for an applied potential $V_{d.c.}$ = -3.5 V at the left electrode L and an ionic strength I = 0.05 mM. **a,** The color map shows the electric potential φ, the red arrows represent the fluid velocity $\mathbf{u}$ and the fluid streamlines at the center electrode C and at the two constrictions. These results were calculated for the trap-in-channel system connected on each side to 25 µm long nanchannels (h = 300 nm) and using the IV-relation shown in Supplementary Fig. 9 and constant surface charge density q_S = 1.0 mC/m^2 as boundary conditions for the electrodes and the channel walls, respectively. The effective surface charge density of the walls is reduced due to double layer interaction with the particle (100 nm in diameter) considered here[16]. At the open ends of the nanochannels, the following boundary conditions were used: φ = 0 V, I = 0.05 mM, pH = 7. **b,** The electrostatic (blue line), pressure related (red line) and drag (orange line) forces for a stationary gold nanoparticle with 100 nm in diameter (surface charge: ~–150*e*). Solving the coupled PNP and NS equations is computationally intensive for the system investigated here (already in 2D) and moving a particle in the trap-in-channel and solving the 3D equations for each position of the particle would have been practically impossible to accomplish within a reasonable time frame. Therefore, we have simulated the 2D system without the particle and used the following approximations $Q_P\mathbf{E}$ (point charge), $\frac{4}{3}\pi R^3 \nabla p$, $6\pi R\eta$ (Stokes) to obtain the electrostatic -, pressure related - and drag forces, respectively, which is a reasonable compromise between accuracy and computational tractability within a context of the present experimental study. **c,** The potential energy *Up* of the particle obtained by spatial integration of the electrostatic and pressure related forces ($U_P = Q_P \int \mathbf{E} d\mathbf{r} + \frac{4}{3}\pi R^3 \int \nabla p d\mathbf{r} = Q_P\varphi + \frac{4}{3}\pi R^3 p$) is shown by the orange line. The effect of the drag force on the particle can be neglected since its magnitude is more than an order of magnitude smaller than the electrostatic force, see (b). For comparison, the potential energy profile of the same gold nanoparticle calculated using the simplified model described in the section Materials and Methods is shown as blue line. The potential energy profiles obtained with the two methods are in fair agreement with each other and, therefore, the simpler model can accurately enough describe the experimental observations of the d.c. mode (Supplementary Fig. 3). The precise calculation using PNP and NS can predict variations in ionic concentrations and fluid flow for an applied potential, but such a study is computationally intensive and the effect of particle geometry cannot be considered. Since the available space for this work is limited and the main goal is dedicated to the experimental results on nanovalving, a comprehensive theoretical and computational analysis and discussion of the d.c. mode using coupled PNP and NS equations will be the topic of a future specialized publication.

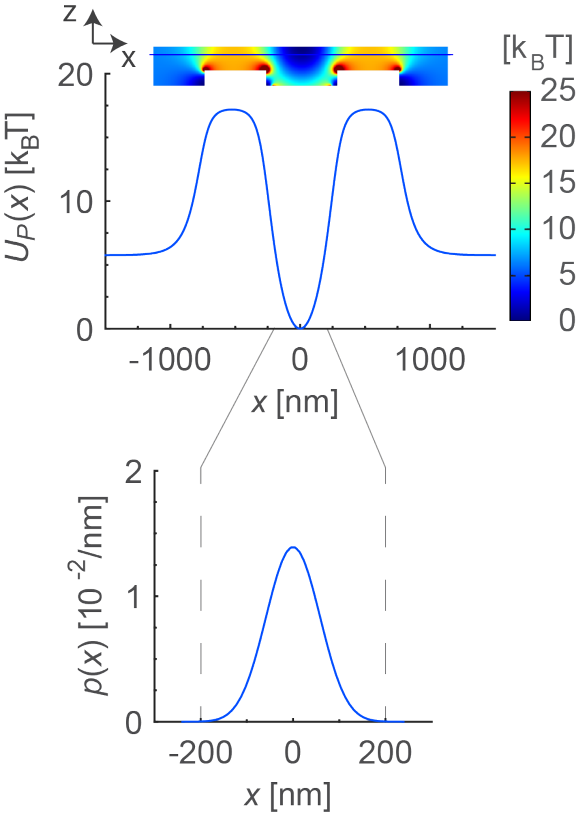

Supplementary Fig. 11. Potential energy and position probability density in a.c.-mode. Potential energy landscape of a 100-nm (diameter) polystyrene particle in the trap-in-channel structure obtained by a two-dimensional (2D) COMSOL simulation of the electric field (equations (5)-(7) in the frequency domain) and employing equation (8). Parameters: $V_{a.c.}$ = 2 V across C-L and C-R electrodes, f = 10 MHz, 0.1X PBS (σ = 0.17 S/m obtained from conductivity measurements) and CM = -0.18. Dimensions were h = 300 nm, s = 500 nm, g = 200 nm and p = 400 nm (Fig. 1a). Potential energy profile $U_P(x)$ and position probability density $p(x)$ are shown of a particle moving along the channel at 70 nm distance from the upper wall (shown by the blue line in the top panel).

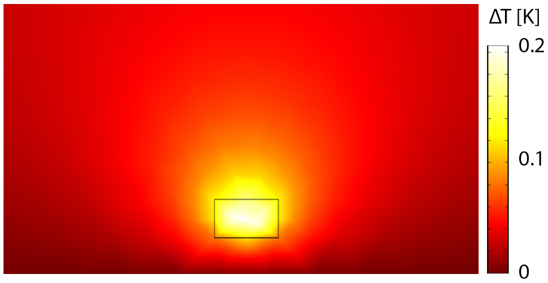

Supplementary Fig. 12. Temperature distribution in the nanovalve from Joule heating. Calculated temperature increase (COMSOL Multiphysics) for a channel (width = 500 nm, height = 300 nm shown by the black rectangle) embedded in a 10 µm thick SiO_2 layer 300 nm above a SiO_2/Si interface for the extreme case of the maximum root-mean-squared electric field strength (E = 1V/µm) and 1X PBS electrolyte (σ = 1.7S/m, maximum conductivity used in our studies). From these values, the heat source in the electrolyte was calculated as $Q_h = 0.5*\sigma\mathbf{E}^2 \approx 10^{12}$ W/m^3. For the simulation $Q_h = 5*10^{12}$ W/m^3 was used to obtain a conservative temperature estimate. The temperature distribution is shown across the channel cross section and in the SiO_2 layer. The SiO_2/Si interface was set to ambient temperature assuming perfect thermal conduction in the Si, and the SiO_2 boundaries were defined as thermal insulators. Despite the conservative conditions simulated, the resulting temperature increase was less than 0.2 K.

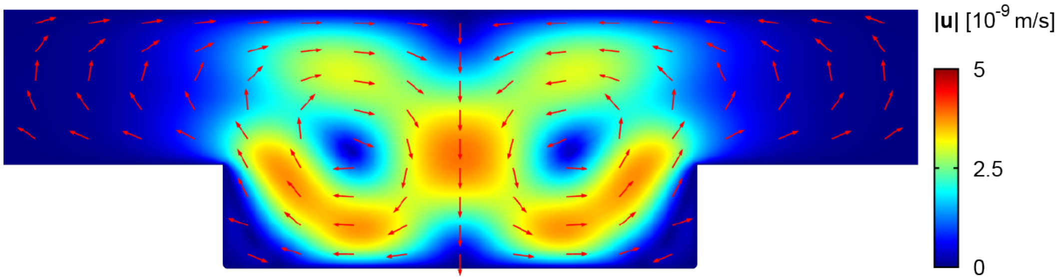

Supplemenary Fig. 13. Electrothermally induced fluid flow in the trap-in-channel system. FEM simulation of the electrothermally induced fluid velocities for the worst case scenario regarding Joule heating at $V = 3$ Va.c. applied at the center electrode and 1X PBS concentration in the a.c. mode. Illustration shows fluid velocities at the center electrode. The calculated fluid velocities are of the order of 10^{-9} m/s which corresponds to a drag force of the order of 10^{-18} N for a particle with 100 nm in diameter using Stokes drag. This is about five orders of magnitude smaller than the repelling force induced by a closed valve ($\approx 10^{-12}$ N).

Supplementary Video Captions

Supplementary Video 1

Controlling the motion of an adenovirus: Guiding, confining and releasing of a single adenovirus (~90 nm in diameter) in biological buffer solution 0.2X PBS (ionic strength: $I \approx 32$ mM) in the a.c. mode (10 MHz) in a trap-in-channel structure. In some instances the video is stopped to explain the opening and closing of the valves.

Supplementary Video 2

Controlling the motion of a gold nanoparticle: Guiding, confining and releasing of a single spherical gold nanoparticle (100 nm in diameter, surface charge: ~-240e) in aqueous solution (I = 0.05 mM) in the d.c. mode in a trap-in-channel structure. The video is stopped to explain the opening and closing of the valves and some parts of the video are slowed down for better visibility of the fast movement of the particle when it enters or exits the trap.

Supplementary Video 3

Controlled sorting of individual quantum dots from an ensemble: Sorting of individual quantum dots (core shell diameter ~10 nm) in biological buffer solution 0.1X borate-buffered saline ($I \approx 16$ mM) in a.c. mode (10 MHz) in a trap-in-junction structure. The video shows the sequences of two single quantum dots guided to the junction and trapped there (thereby isolated from the ensemble), and then released to the left (the first quantum dot) or right (the second quantum dot) branch, respectively. In some instances the video is stopped to explain the opening and closing of the valves.

Supplementary Video 4

Controlled sorting of individual immunoglobulin G antibodies from an ensemble: Sorting of individual immunoglobulin G antibodies (144 kDa) in biological buffer solution 0.1X PBS ($I \approx$ 16 mM) in a.c. mode (10 MHz) in a trap-in-junction structure. The video shows the sequences of two single immunoglobulin G antibodies guided to the junction and trapped there (thereby isolated from the ensemble), and then released to the left (the first antibody) or right (the second antibody) branch, respectively. In some instances the video is stopped to notify the viewer of the opening and closing of the valves. The immunoglobulin G antibodies were imaged at a frame rate of 33.8 Hz.

Supplementary Video 5

Controlled sorting of individual adenoviruses: Sorting of individual adenoviruses (~90 nm in diameter) in biological buffer solution 0.2X PBS ($I \approx$ 32 mM) in a.c. mode (10 MHz) in a trap-in-junction structure. The video shows the sequences of two single viruses guided to and trapped at the junction, and then released to the left (the first virus) or right (the second virus) branch, respectively. In some instances the video is stopped to explain the opening and closing of the valves.

Supplementary Video 6

Controlling the motion of a single gold nanoparticle in a trap-in-junction structure: A gold nanoparticle (100 nm in diameter) in aqueous solution ($I = 0.05$ mM) is controlled in d.c. mode: it is guided to the trap, confined there, released to a selected branch and then brought back to the trap. This sequence is repeated for each branch with the same particle. In some instances the video is stopped to explain the opening and closing of the valves and some parts of the video are slowed down for better visibility of the fast movement of the particle.

Supplementary Video 7

On-demand trapping of two individual nanoparticles in a trap-in-junction structure: Two fluorescent beads (100 nm in diameter) and two gold nanoparticles (100 nm in diameter) are controlled in biological buffer solution 0.1X PBS ($I \approx 16$ mM) and aqueous solution ($I = 0.05$ mM), respectively, using the a.c. (10 MHz) and the d.c. modes. For each particle type, the video shows that, while a particle is trapped, a second particle is loaded on-demand into the same trap-in-junction structure. In some instances the video is stopped to explain the opening and closing of the valves.

Supplementary References

1. Ai, Y. & Qian, S. Electrokinetic particle translocation through a nanopore. *Phys. Chem. Chem. Phys.* **13,** 4060–71 (2011).

2. Morgan, H. & Green, N. G. *AC Electrokinetics: Colloids and Nanoparticles*. (Research Studies Press, 2003).

3. Ghonge, T., Chakraborty, J., Dey, R. & Chakraborty, S. Electrohydrodynamics within the electrical double layer in the presence of finite temperature gradients. *Phys. Rev. E* **88,** 53020 (2013).

4. Banerjee, A. & Kihm, K. D. Experimental verification of near-wall hindered diffusion for the Brownian motion of nanoparticles using evanescent wave microscopy. *Phys. Rev. E* **72,** 42101 (2005).

5. Eichmann, S. L., Anekal, S. G. & Bevan, M. a. Electrostatically confined nanoparticle interactions and dynamics. *Langmuir* **24,** 714–721 (2008).

6. Unger, M. a, Chou, H. P., Thorsen, T., Scherer, a & Quake, S. R. Monolithic microfabricated valves and pumps by multilayer soft lithography. *Science* **288,** 113–116 (2000).

7. Thorsen, T., Maerkl, S. J. & Quake, S. R. Microfluidic Large-Scale Integration. *Science* **298,** 580–584 (2002).

8. Chen, Y. W. *et al.* Atomic layer-deposited tunnel oxide stabilizes silicon photoanodes for water oxidation. *Nat. Mater.* **10,** 539–544 (2011).

9. Harrer, S. *et al.* Electrochemical protection of thin film electrodes in solid state nanopores. *Nanotechnology* **22,** 275304 (2011).

10. Harrer, S. *et al.* Electrochemical characterization of thin film electrodes toward developing a DNA transistor. *Langmuir* **26,** 19191–19198 (2010).

11. Schuegraf, K. F. & Hu, C. Hole Injection Si02 Breakdown Model for Very Low Voltage Lifetime Extrapolation. *IEEE Trans. Electron Devices* **41,** 761–767 (1994).

12. Savin, T. & Doyle, P. S. Role of a finite exposure time on measuring an elastic modulus using microrheology. *Phys. Rev. E - Stat. Nonlinear, Soft Matter Phys.* **71,** 6–11 (2005).

13. Libchaber, A. & Simon, A. Escape and Synchronization of a Brownian Particle. *Phys. Rev. Lett.* **68,** 3375–3378 (1992).

14. Burg, B. R., Bianco, V., Schneider, J. & Poulikakos, D. Electrokinetic framework of dielectrophoretic deposition devices. *J. Appl. Phys.* **107,** 1–11 (2010).

15. Bazant, M., Chu, K. & Bayly, B. J. Current-voltage relations for electrochemical thin films. *SIAM J. Appl. Math.* **65,** 1463–1484 (2005).

16. Behrens, S. H. & Grier, D. G. The charge of glass and silica surfaces. *J. Chem. Phys.* **115,** 6716–6721 (2001).